

Particle Size Effects in the Catalytic Electroreduction of CO₂ on Cu Nanoparticles

Rulle Reske,^{†,||} Hemma Mistry,^{‡,||} Farzad Behafarid,[‡] Beatriz Roldan Cuenya,^{*,§} and Peter Strasser^{*,†}

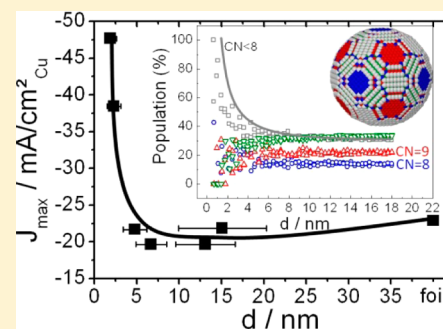
[†]Department of Chemistry, Chemical Engineering Division, Technical University Berlin, 10623 Berlin, Germany

[‡]Department of Physics, University of Central Florida, Orlando, Florida 32816, United States

[§]Department of Physics, Ruhr-University Bochum, 44780 Bochum, Germany

S Supporting Information

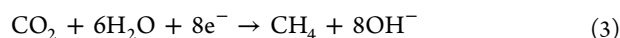
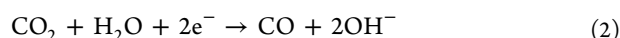
ABSTRACT: A study of particle size effects during the catalytic CO₂ electroreduction on size-controlled Cu nanoparticles (NPs) is presented. Cu NP catalysts in the 2–15 nm mean size range were prepared, and their catalytic activity and selectivity during CO₂ electroreduction were analyzed and compared to a bulk Cu electrode. A dramatic increase in the catalytic activity and selectivity for H₂ and CO was observed with decreasing Cu particle size, in particular, for NPs below 5 nm. Hydrocarbon (methane and ethylene) selectivity was increasingly suppressed for nanoscale Cu surfaces. The size dependence of the surface atomic coordination of model spherical Cu particles was used to rationalize the experimental results. Changes in the population of low-coordinated surface sites and their stronger chemisorption were linked to surging H₂ and CO selectivities, higher catalytic activity, and smaller hydrocarbon selectivity. The presented activity–selectivity–size relations provide novel insights in the CO₂ electroreduction reaction on nanoscale surfaces. Our smallest nanoparticles (~2 nm) enter the ab initio computationally accessible size regime, and therefore, the results obtained lend themselves well to density functional theory (DFT) evaluation and reaction mechanism verification.



1. INTRODUCTION

Carbon dioxide (CO₂) is a greenhouse gas which is produced by the burning of fossil fuels for energy generation and transportation, and through industrial processes such as concrete production. Due to the world's growing energy demands, rising CO₂ emissions are a serious environmental threat. To mitigate this, closing the anthropogenic carbon cycle through a chemical conversion of CO₂ into usable chemicals would be an attractive solution.¹ Such methods would involve the utilization of waste CO₂ as a chemical feedstock² to make hydrocarbons, alcohols, or CO-rich feeds of high interest for industry. Of all chemical ways to convert CO₂ into useful products, the electrocatalytic route appears as the most sustainable as it occurs at ambient pressures and temperatures, in neutral pH conditions, catalyzed by non-noble metals, and may involve renewable electricity from wind, solar, or hydro power plants.

It is well-known^{3,4} that CO₂ can be electrochemically reduced on copper surfaces in aqueous solutions, producing formate, CO, and hydrocarbons like methane (CH₄) and ethylene (C₂H₄) according to



Although the standard potentials of CO₂ reduction to CH₄ or C₂H₄ are small and positive ($E^0_{\text{CH}_4} = +0.169$ V vs the standard hydrogen electrode (SHE) and $E^0_{\text{C}_2\text{H}_4} = +0.079$ V vs SHE),^{5,6} the over potential of these reactions are in a range of –800 to –900 mV,^{6–10} which makes these processes energetically very inefficient. Furthermore, the catalytic selectivities of hydrocarbons are generally relatively small compared to the formation of molecular hydrogen according to $2\text{H}_2\text{O} + 2\text{e}^- \rightarrow \text{H}_2 + 2\text{OH}^-$ ($E^0_{\text{H}_2} = 0$ V versus the reversible hydrogen electrode, RHE).

In the past few years, several studies have investigated the mechanism of the CO₂ reduction reaction.^{9,11–14} It is generally accepted that carbon monoxide (CO) is an intermediate in the reduction of CO₂. Density functional theory (DFT) calculations put forward by the Norskov group proposed that the protonation of the adsorbed CO to CHO* is the potential determining step (PDS) of methane formation on (211) and (100) surfaces.^{9,14} On (111) surfaces, the initial protonation of CO₂ was predicted to dictate the potential requirements. By the same authors, ethylene was predicted to form through a chemical dimerization step of CHO or similar adsorbates. Schouten et al.^{12,13} demonstrated experimentally that the Cu(100) surface offers a uniquely active reaction pathway for the formation of C₂H₄ via an electron-mediated dimerization reaction of two adsorbed CO molecules. Dimerization of CO

Received: January 12, 2014

Published: April 18, 2014

Table 1. Parameters Used in the Synthesis of Size-Controlled Micellar Cu NPs^a

sample name	polymer	loading	no. of coats	particle size h_p (nm)	real Cu surface area $A_{Cu, norm}$ (cm ² _{Cu} /cm ² _{geo})
S1	PS(26000)-P2VP(4800)	0.2	4	1.9 ± 0.7	0.018 ± 0.001
S2	PS(27700)-P2VP(4300)	0.4	4	2.3 ± 0.8	0.037 ± 0.002
S3	PS(33000)-P2VP(46000)	0.4	3	4.8 ± 1.4	0.110 ± 0.005
S4	PS(33000)-P2VP(46000)	0.4	5	6.7 ± 1.8	0.153 ± 0.008
S5	PS(130000)-P2VP(135000)	0.1	5	13.1 ± 3.5	0.06 ± 0.01
S6	PS(130000)-P2VP(135000)	0.4	5	15.1 ± 5.2	0.07 ± 0.02

^aMolecular weight of the PS-P2VP polymers, metal-salt to polymer-head ratio (loading), AFM heights with error bars (standard deviation) measured on SiO₂/Si(111) supported NPs, and normalized Cu surface areas calculated from the AFM heights as surface area of NPs/geometric surface area of support, assuming spherical NPs.

on Cu(111) indeed was unfavorable compared to the protonation of CO to COH.^{9,11,14} More recently, Nie et al.¹¹ proposed that methane and ethylene formation on Cu(111) occurs via a common hydroxyl–methylidyne intermediate, *C–OH, which is subsequently hydrogenated to a common CH₂* intermediate. That latter adsorbate may undergo a nonelectrochemical dimerization and C–C bond formation toward ethylene or else hydrogenate further to methane.¹¹

Controlling the selectivity of the CO₂ reduction reaction and reducing the over potential for the formation of methane and ethylene are currently major scientific challenges. The geometry, morphology, and roughness of copper single crystal and polycrystalline surfaces have shown a dramatic influence on the catalytic activity and product selectivity during CO₂ electroreduction.^{7,10,15} Enhanced ethylene and CO formation was reported on roughened Cu foils.¹⁰ The altered selectivity was rationalized based on differences in the chemisorption characteristics of (111), (100), and (211) surfaces. DFT calculations confirmed that key intermediates, such as *CO and *CHO were stabilized on stepped surfaces owing to more negative chemisorption energies. Vollmer et al. used temperature-programmed desorption (TPD) to study CO adsorption on (i) low index surfaces (Cu(111), Cu(100), and Cu(110)), (ii) stepped and kinked surfaces (Cu(211), Cu(221), and Cu(532)), and on (iii) sputtered and polycrystalline Cu films, concluding that CO binds more strongly on Cu step edges and kinks than on terrace sites.¹⁶

Chemisorption and catalytic selectivities can also be controlled by lattice strain in thin metal overlayers.^{17–20} This was shown in the electroreduction of CO₂ on thin Cu overlayers on Pt studied using online electrochemical mass spectrometry (OLEMS).²¹ Results showed that by decreasing the copper overlayer thickness, the selectivity of C₂H₄ versus CH₄ increased, while the activity decreased.²¹ This was explained by the alteration of the chemisorption of reactive intermediates due to geometric lattice effects.

Another well-known morphology-based strategy to tune surface chemisorption and resulting catalytic activities and selectivities is varying the size and/or shape of the catalytically active species, for instance, metal nanoparticles (NPs).^{22,23} Utilized in practice for centuries, this dispersion dependence is generally known as the “catalytic particle size effect”.^{24–28} For very small NP diameters below around 2 nm, where quantum effects become noticeable,^{28–30} the effect is often also referred to as the “catalytic finite-size effect”.²⁸ Size effects have frequently been reported for gas-phase catalytic reactions on metal NPs, such as hydrogenations,^{31–33} ammonia synthesis,³⁴ alcohol decomposition reactions,³⁵ or partial oxidation reactions,^{36–46} and CO oxidation on Au NPs is the most prominent example.^{47,48} Electrocatalytic reactions where size

effects have been explored include the oxygen reduction reaction on noble metals,^{23,49–54} the electro-evolution of molecular oxygen,^{55–58} and electro-oxidation of small organic molecules,⁵⁹ as well as electrocatalytic CO oxidation.^{60–62} The oxygen electroreduction reaction (ORR) on Pt, for instance, exhibits a pronounced particle size effect: Plotted against the particle diameter, the Pt mass-based catalytic activity shows a nonmonotonic dependence with a maximum activity for Pt NPs between 3 and 5 nm in size.^{49,52,63,64} To date, reports on NP size effects involving Cu NPs have been limited to heterogeneously catalyzed gas-phase reactions, such as the heterogeneous oxidation of CO in an excess of hydrogen and the catalytic degradation of gaseous carbon tetrachloride.^{65,66} The present study is the first exploration of catalytic particle size effects in CO₂ electroreduction on Cu NPs.

Here, we investigate the influence of the size of Cu NPs on the CO₂ electroreduction activity and, in particular, on product selectivity. The copper NPs ranged from 2 to 15 nm in size and gave rise to unexpected selectivity and activity variations. Aside from providing a practical strategy for deliberately altering activity and product selectivity, this size effect study provides new clues and hypotheses how chemical bonding controls the selectivity in CO₂ electro conversion. Experimental materials, reaction conditions, observables, and their interpretation lend themselves easily to theoretical verification and thus will add important aspects to a more complete mechanistic understanding of such an important energy storage reaction.

2. EXPERIMENTAL METHODS

2.1. Sample Preparation. Size-selected Cu NPs were prepared via inverse micelle encapsulation. Poly(styrene)-*block*-poly(2-vinylpyridine) (PS-P2VP) diblock copolymers (Polymer Source, Inc.) with polar head (PVP) and nonpolar tail (PS) blocks were dissolved in nonpolar toluene to form inverse micelles. The micelles were then loaded with CuCl₂ and stirred for 2 days to form monodispersed Cu NPs. The size of the NPs is controlled either by varying the molecular weight of the PVP head or by varying the metal salt/PVP ratio. By varying these two parameters, five different solutions were prepared, see Table 1. Glassy carbon plates were dip-coated into the solution, resulting in a monolayer of NPs deposited on the support. The molecular weight of the polymer tail can be varied to control interparticle spacing. Next, the encapsulating polymers were removed by O₂ plasma etching for 20 min (20 W power). To increase the NP density, the dip-coating and plasma etching (ligand removal) steps were successively repeated 3–4 times on each individual sample. NPs were simultaneously prepared on flat SiO₂(4 nm)/Si(111) supports and underwent the same treatment as the glassy carbon supported NPs. The complete removal of polymeric ligands from Cu/SiO₂/Si(111) samples was demonstrated based on the lack of any C-1s signal in high resolution XPS measurements (Supporting Information Figure S1). However, such measurements are not possible for Cu NPs supported on glassy carbon due to the very strong carbon

signal from the support. Nevertheless, since similar micelle prepared NPs (same NP solution) were deposited on both SiO₂/Si(111) and glassy carbon supports, and since the same plasma treatment procedure was carried out on both samples, the complete removal of the polymeric ligands is guaranteed from our XPS measurements on SiO₂/Si(111).

Detailed information on the parameters used for the synthesis of the Cu NPs is listed in Table 1.

2.2. Sample Characterization. Atomic force microscopy (AFM) images acquired in tapping-mode (Digital Instruments Nanoscope III) were used to characterize the NP morphology on SiO₂(4 nm)/Si(111). Average AFM particle heights h_p (size) and support area-normalized NP surface areas, $A_{Cu, norm}$ (in units of cm²_{Cu}/cm²_{geo}), were calculated assuming spherical particles, Table 1. Histograms of the NP heights obtained by AFM for all samples are shown in Supporting Information Figure S2. The assumption of a spherical NP shape on weakly interacting supports such as SiO₂ or C is based on previous cross sectional transmission electron microscopy studies on similarly synthesized NPs.⁶⁷ The surface area of a single particle A_p was estimated according to $A_p = 4\pi(h_p/2)^2$. Using the surface particle density on the flat support, $A_{Cu, norm}$ was evaluated.

To corroborate the accuracy of the NP sizes (height) obtained via AFM for our samples containing small NPs, an equivalent of sample S1 was also measured via transmission electron microscopy (TEM) with a FEI Tecnai 20 microscope operated at 200 kV. For the TEM study, Cu NPs analogous to those in sample S1 (same NP solution) were drop-coated on a 40 nm-thick SiO₂ TEM grid, and the encapsulating ligands were removed via O₂-plasma exposure. The TEM image of this sample and the corresponding size histogram are shown in Supporting Information Figure S3. The average diameter obtained from TEM is 2.4 ± 0.6 nm, in relatively good agreement with the average size (NP height) obtained via AFM (1.9 ± 0.7 nm).

2.3. Electrochemical Measurements of the CO₂ Reduction. An airtight electrochemical cell with a three-compartment, three-electrode design was used for the electrochemical CO₂ reduction. The glassware was cleaned in a “nochromix” bath and afterward in concentrated HNO₃ for 1 h, respectively, rinsed with ultra pure water several times, and dried at $T = 60$ °C in a drying cabinet. A platinum mesh 100 (Sigma-Aldrich 99.9%) formed to a cylinder was used as counter electrode (CE) and a leak-free Ag/AgCl electrode as reference electrode (Hugo Sachs Elektronik Harvard apparatus GmbH).

The glassy carbon plate, on which the Cu NPs were supported, was contacted with a gold clamp and used as working electrode (WE). The geometric surface area, A_{geo} , of the particle-covered support was 3 cm². Twenty-five milliliters of 0.1 M KHCO₃ (Roth >99.5%) was used as electrolyte and purged with CO₂ (Air liquid 4.5) (30 mL/min) from the bottom of the cell under the WE until a final stable pH of 6.8 was reached.³ Before and during the electrochemical measurements, the CO₂ saturation of the gas atmosphere was controlled with an in situ mass spectrometer (OmniStar GSD 301c, Pfeiffer). Hydrogen (H₂), carbon monoxide (CO), methane (CH₄), and ethylene (C₂H₄) were analyzed using a gas chromatography (GC) system protocol detailed in Figure S4 of the Supporting Information. The gas chromatograph used was a Shimadzu GC 2016 equipped with a thermal conductivity detector (TCD) and a flame ionization detector (FID). Argon (Air liquid 5.0) was employed as carrier gas. The gaseous products H₂, N₂, O₂, CH₄ and CO were separated in a molecular sieve column (Alltech, part no. 57732, 1.65 m × 1/8 in., molecular sieve 13X, 60/80 mesh) and for C₂–C₃ hydrocarbons and CO₂ in a HayeSep column (Alltech, part no. 14487, 3.5 m × 1/8 in., HayeSep D, 80/100 mesh).

The working electrodes were always immersed into the electrolyte under potential control at $E = +0.22$ V/RHE. A linear voltammetric sweep was performed with a scan rate of -5 mV/s between $E = +0.22$ V/RHE and $E = -1.1$ V/RHE followed by a chronoamperometric measurement at $E = -1.1$ V/RHE for $t = 10$ min. At the end of the amperometric step, product gas samples were analyzed. CO₂ gas was bubbling through the electrochemical cell throughout the electrochemical measurements to ensure sufficient convective mass transport to keep the Nernst diffusion layer thicknesses to a minimum and minimize mass transport limitations and local pH changes at the

electrode interface. All potentials are reported with respect to the reversible hydrogen electrode (RHE) and were corrected by the experimental voltage loss (IR-drop) caused by the uncompensated resistances of the electrolyte and external electrical contacts and connections. ICP-OS measurements of Pt ion concentration before and after the electrochemical experiments showed no detectable evidence of dissolved Pt ions, confirming the lack of any significant dissolution of the Pt anode (counter electrode) during the experiments. In addition, high-resolution XPS measurements confirmed the absence of Pt on the Cu foil or Cu NPs after electrocatalysis, ruling out any possibility of Pt ion cross contamination.

Cu surface-area normalized catalytic activity and selectivity values were calculated from raw current data subtracting coverage-corrected current and selectivity values of bare glassy carbon supports, followed by subsequent division by the real Cu surface area, $A_{Cu, norm} \times A_{geo}$, of the Cu NPs according to Table 1.

2.4. Numerical Calculation of Model Nanoparticles. To generate spherical Cu NP model shapes, a large FCC structure with a Cu lattice unit (L) of 3.61 Å was constructed using a MATLAB code. When the desired diameter was varied, all the atoms outside the defined sphere were removed from the bulk FCC structure in order to construct each model shape. For the database to be comprehensive, different symmetry centers (SC) were considered with (i) the SC located on one of the Cu atoms and (ii) the SC shifted 0.5L along one of the Cartesian axes (e.g., x -axis). The largest spherical NP considered had a diameter of 18 nm and about 261000 atoms. The relation between the number of Cu atoms and the NP diameter is shown in Supporting Information Figure S5a.

In the next step, for each model shape in the database, the coordination number (CN) of all individual atoms was calculated. Atoms with a CN value of 12 were considered as bulk atoms and those with CN below 12 were considered as surface atoms. Supporting Information Figure S5b shows the percentage of surface and bulk atoms as a function of the NP diameter. The surface atoms were also further distinguished based on their coordination number as will be discussed later.

3. RESULTS

3.1. Synthesis and Structural Characterization of Cu NP Catalysts. A well-established micelle-based nanoparticle preparation method^{48,68–70} was utilized to prepare six metallic Cu NP catalysts with spherical shape and different, well-controlled particle height (“size”), henceforth referred to as S1 to S6 in order of increasing size, Table 1. This synthesis method has been known to produce highly reproducible particle sizes, and multiple duplicates of all six NP catalysts were prepared and measured independently. Figure 1 shows AFM images of the spherical Cu NPs after ligand removal.

Analysis of the AFM particle heights revealed that six distinct average NP sizes between 1.9 and 15.1 nm were obtained (see Table 1). Particle size histograms, shown in Supporting Information Figure S2, evidenced largely near-symmetric, narrow size distributions. Increasing the molecular weight of the micelle head or increasing the metal loading inside the micelles generally resulted in larger NP sizes. The interparticle distance generally decreased with smaller NP size due to the successive multiple dip-coatings employed in the preparation of such samples in order to ensure sufficient active Cu NP surface and coverage on the carbon support.

3.2. Electrocatalytic Activity Measurements. The Cu NP catalysts S1–S6 were supported on flat glassy carbon electrodes and were subsequently deployed as working electrode in a three-electrode electrochemical setup designed for the electroreduction of CO₂ in a 0.1 M bicarbonate solution at pH 6.8.³ The activity and chemical selectivity of catalysts

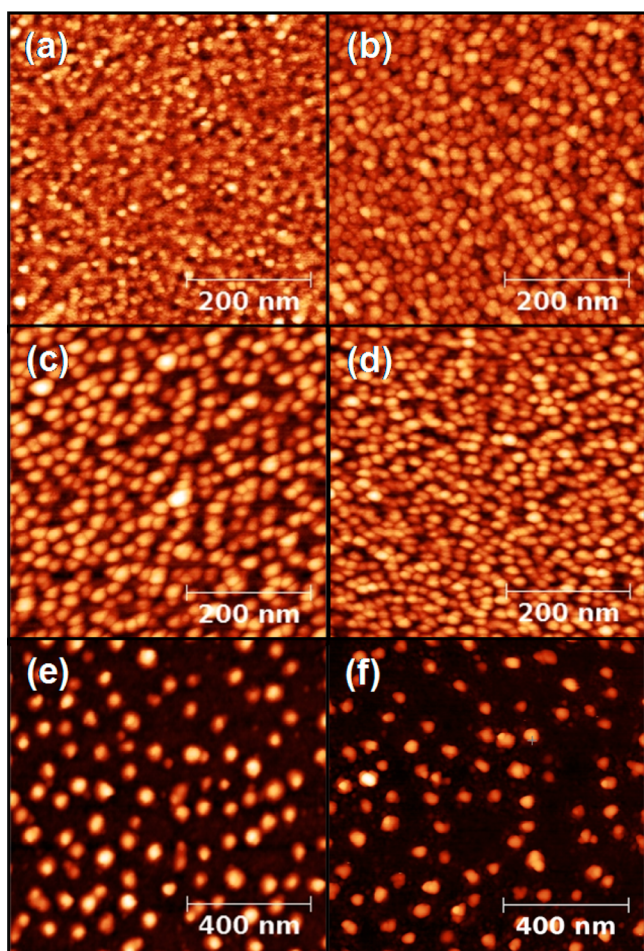


Figure 1. Tapping-mode AFM images of micellar Cu NPs: (a) S1, (b) S2, (c) S3, (d) S4, (e) S5, and (f) S6.

S1–S6 for CO₂ electroreduction were monitored during a slow cathodic potential scan as well as at a constant electrode potential of -1.1 V/RHE. Reproducibility of individual catalytic activity was confirmed and sample averages are provided. Figure 2 displays the Linear Sweep Voltammograms (LSV) of

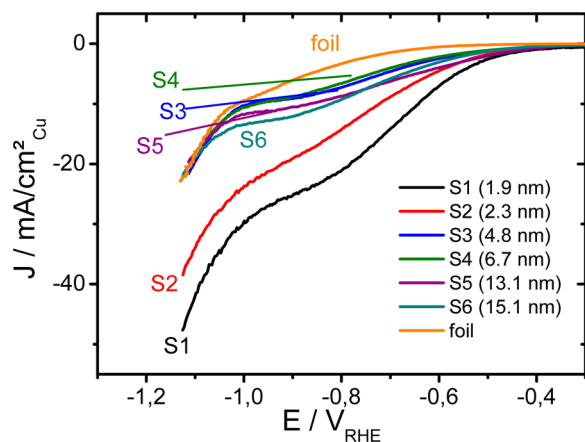


Figure 2. Linear sweep voltammetry of the CO₂ electroreduction on Cu NP catalysts, S1–S6, in 0.1 M KHCO₃ acquired at room temperature with -5 mV/s scan rate. Current densities are normalized by the Cu particle surface area after subtraction of the glassy carbon background signal. A Cu foil electrode (“foil”) is included as reference.

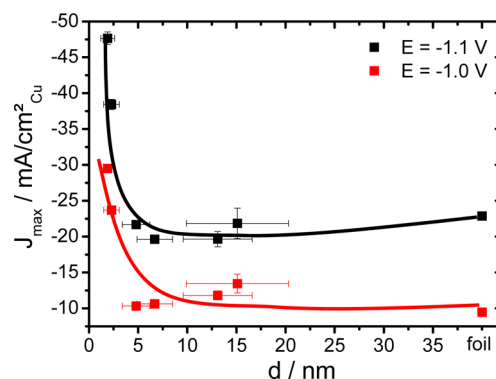


Figure 3. Particle size effect during catalytic CO₂ electroreduction. The faradaic current densities at -1.1 and -1.0 V/RHE are plotted against the size of the Cu NP catalysts. The current densities have been normalized by the Cu particle surface area after subtraction of the glassy carbon background signal. Error bars indicate scatter in particle size distributions. Lines are guides to the eye. Data of a Cu foil electrode (“foil”) are inserted as reference. Conditions: 0.1 M KHCO₃, pH = 6.8, 25 °C.

each Cu NP catalyst in comparison to the LSV of a Cu foil electrode (“foil”), which was considered an extended macroscopic Cu reference catalyst. To correct for differences in the electrochemically active real surface area of each Cu NP catalyst, the geometric current density was converted into the Cu surface area-specific current density after the subtraction of the glassy carbon (support) background.

Figure 2 reveals a dramatic particle size effect on the overall catalytic CO₂ electroreduction activity of Cu NPs. The LSV of the Cu foil showed the characteristic shoulder between -0.8 and -1.0 V, previously associated with the formation of carbonous surface species. The catalytic LSV currents of the Cu bulk reference in Figure 2 are in excellent quantitative agreement with previous reports of CO₂ reduction on Cu foil electrodes in buffered bicarbonate solutions.^{3–5,71} The total current of the Cu foil at -1.1 V/RHE was -23 mA/cm², while that reported by Hori⁴ under similar conditions was -25 mA/cm².

In stark contrast to the Cu foil electrode, the Cu NPs exhibited significantly higher catalytic activity (larger negative current density J) as the Cu NP size decreased. The smallest Cu NPs (S1 and S2, ~ 2 nm) showed almost twice the catalytic activity of extended bulk Cu, while catalysts S3–S6 exhibited similar catalytic activities over a wide potential window, ranging between those of bulk Cu and of S2. Electrochemical Tafel lines of the NP electrocatalysts are plotted in Supporting Information Figure S6 evidencing similar slopes and curvatures in the -0.4 to -0.8 V range, yet a clearly more pronounced activity plateau in the -0.8 to -1.0 V range.

Figure 3 highlights the dependence of the overall catalytic CO₂ reduction activity on particle size at two different electrode potentials, $E = -1.1$ V/RHE and $E = -1.0$ V/RHE (detailed activity values are given in Supporting Information Table S1). The data suggest comparable overall activity between bulk Cu and Cu NPs down to about 5 nm, below which an explosive trend toward higher catalytic activity with smaller Cu NP size becomes evident. The smallest Cu NP catalyst (1.9 nm) displayed a 100% increase in faradaic current density (-48 mA/cm²_{Cu}; see Supporting Information Table S1), while the 2.3 nm NP catalyst S2 still showed a 50% increase in activity compared to Cu foil electrode. Together, the observed trends evidence a

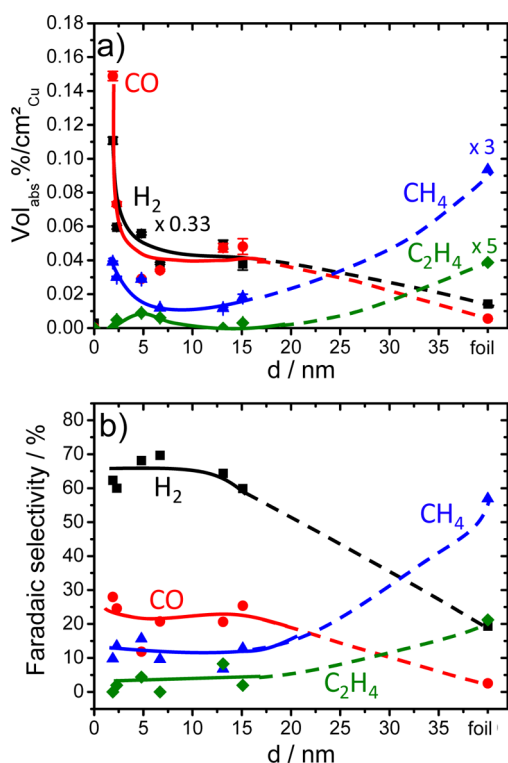


Figure 4. Particle size dependence of (a) the composition of gaseous reaction products (balance is CO₂) during catalytic CO₂ electroreduction over Cu NPs, (b) the faradaic selectivities of reaction products during the CO₂ electroreduction on Cu NPs. Lines are guides to the eye. Conditions: 0.1 M KHCO₃, $E = -1.1$ V/RHE, 25 °C. For (a), volume concentrations were normalized using the Cu surface areas. Values for H₂, CH₄, and C₂H₄ are scaled by factors of 0.33, 3, and 5, respectively.

dramatic activity-enhancing size effect of nanoscale spherical Cu surfaces during CO₂ reduction.

3.3. Electrochemical Selectivity Measurements. To obtain insight into the relevant catalytic reaction pathways, faradaic selectivity measurements were performed under stationary reaction conditions at -1.1 V/RHE. Supporting Information Table S1 and Figure 4a report the background-corrected, NP surface area-normalized product composition of the gas stream leaving the working electrode compartment. Each data point represents the average of at least three independent measurements. The excess CO₂ flow keeps the combined volumetric ratios of gas reaction products below 1 vol % for all NP sizes (note that the values of three products are scaled with the factor given in the plot). We note that the absolute volume % values (gas molar ratios) of the reaction products are sensitive to variations in the volumetric CO₂ flow, a shortcoming which is eliminated when relative faradaic selectivities are considered.

It is evident from Figure 4a that major reaction products were hydrogen, CO, methane, and ethylene. While a minute amount of liquid formic acid was detectable for the Cu foil (<5% consistent with ref 4), no detectable quantities of formic acid were formed for the nanoparticle samples.

The size of the Cu NP catalysts had a significant effect on the formation rate of individual products and, hence, their catalytic selectivity. Larger particles in the 5–15 nm size regime clearly showed much less hydrocarbon formation, and instead yielded more H₂ and CO. Smaller particles below 5 nm displayed a

sudden increase in H₂ and CO formation relative to hydrocarbons. It is evident that small Cu NPs, in stark contrast to bulk Cu surfaces, evolve no significant amounts of the highly desired reaction product ethylene.

Taking the number of transferred electrons of each species into consideration, the volumetric ratios were converted into faradaic selectivities, see Figure 4b. We note that the faradaic selectivities of the Cu bulk electrode are in good agreement with earlier reports by Hori.⁴ Methane showed the highest selectivity of 57% (55% reported by Hori), ethylene and hydrogen showing about 20% (25% and 10% reported by Hori), and CO exhibiting less than 5% selectivity (3% reported by Hori).

The data in Figure 4b evidence a drastic dependence of the product selectivities on the size of the spherical Cu NP catalysts at a given overpotential. In contrast to the bulk Cu electrode, the selectivity profiles of Cu NPs are largely dominated by hydrogen evolution (60–70% compared to 20% on Cu bulk) over the entire size range considered, a pattern that typically occurs for extended Cu bulk surfaces at much less negative overpotentials. The selectivities of methane and ethylene dropped drastically from their bulk values to much reduced levels (10–15% for methane and 0–10% for ethylene) in the 5–15 nm particle size regime, while CO selectivities followed the trend of hydrogen and increased from 5% to 20–25%. The anticorrelation between methane and ethylene, on the one hand, and H₂ and CO, on the other, is quite obvious in Figure 4b. At particle sizes below 5 nm, hydrocarbon selectivities dropped again with ethylene formation ceasing on 1.9 nm Cu particles. At the same time, CO selectivity increased to almost 30%.

3.3. Modeling Surface Atomic Coordination of Spherical Cu NPs. To gain insight into the origin of the observed particle size effects, model spherical Cu NPs between 1 and 18 nm diameter were considered with a face-centered cubic structure and a unit cell parameter of $a = 3.610$ Å. Figure 5a illustrates the surface structure of 2.2 nm (left) and 6.9 nm (right) NPs corresponding to catalysts S2 and S4. The percentage ratio of the surface atoms with specific nearest-neighbor coordination numbers (CN) between 5 and 11 were considered and binned into atoms with CN < 8, CN = 8, CN = 9, and CN > 9. Figure 5b breaks down the size-dependent populations of atoms with these four CN groups.

Atoms with coordination 8 (blue), 9 (red), and >9 (green) accounted together for about 70% of the surface atoms of spherical particles between 6 and 18 nm. The contribution of low coordinated atoms (steps and kinks) (gray) increased slightly between 18 and 6 nm, then started to become significant between 6 and 2 nm, and finally drastically augmented for NPs below 2 nm. Below 4 nm, the scatter in the individual populations increased considerably, until, below 2 nm, low-coordinated steps prevailed on the surface of the Cu NPs. The color coding in Figure 5a reflects the location of atoms with individual CN providing an intuitive picture of how the individual CNs are distributed across the surface of the particles. Atoms in Cu(111) and Cu(100) surfaces have CN values of 9 (red) and 8 (blue), respectively. Also the second layer of atoms in Cu(110) and Cu(211) surfaces have CN of 11 and 10, respectively (green). However, there are a small number of atoms with the mentioned CN values that do not belong to the assigned Cu surface orientation (e.g., 6 blue-colored kink atoms with CN = 8 at the corner of each 111 facet). Nevertheless, the color coding illustrates the complexity

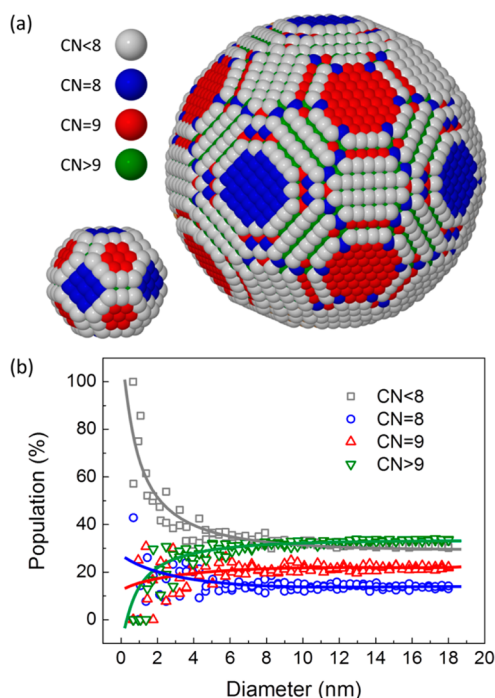


Figure 5. (a) Ball models of spherical Cu NPs with 2.2 and 6.9 nm diameters. Surface atoms are color-coded according to their first neighbor coordination number (CN), CN < 8 (gray), CN = 8 (blue), CN = 9 (red), CN > 9 (green). (b) Population (relative ratio) of surface atoms with a specific CN as a function of particle diameter.

of the surface atomic coordination on such spherical particles compared to faceted Wulff-type models (truncated cuboctahedron shape).

4. DISCUSSION

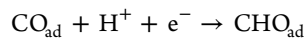
Structure sensitivity is very common in homogeneous, heterogeneous, electro-, and biocatalysts. However, the dependence of the catalytic activity and selectivity on the *catalyst dispersion* is an idiosyncrasy of heterogeneous catalysts and heterogeneously catalyzed reactions.

This study has explored the effect of the size of spherical Cu NPs on the catalytic activity and selectivity during the mechanistically fairly complex electrocatalytic reduction of CO₂. It is the first of its kind for Cu and CO₂ electrocatalysis, and has revealed a distinctly different behavior of nanoscale Cu surfaces compared to their extended bulk counterparts. A significant increase in the overall faradaic activity was found with shrinking NP size. This was coupled to an increased selectivity for hydrogen and CO, but decreased selectivity for hydrocarbon production. Entering the smallest size domains of particles below 3 nm, hydrocarbon formation drops drastically, while CO is the preferred carbonaceous product.

4.1. Stepped Extended Surfaces. Stepped extended surfaces have often been considered as models for the behavior of particle surfaces. The effect of steps and kinks on well-defined planar Cu surfaces on the catalytic activity and selectivity of CO₂ electroreduction has first been addressed by Hori and co-workers.^{3,72} They reported a high selectivity for ethylene on Cu(100), while methane formation was clearly preferred on Cu(111) facets. Steps in (100) terraces, regardless of their orientation, increased the ethylene formation over methane. Hori's observations were later confirmed by Koper and co-workers,^{12,13} who found Cu(100) to be highly active

and selective for ethylene and proposed a decoupled proton–electron transfer during a dimerization of CO to explain the pH independence of the reaction. More recently, surface morphology effects in CO₂ electroreduction were explored by Tang et al.,¹⁰ who found that steps on roughened Cu surfaces show increased ethylene, but very low methane selectivity. Unlike Hori, however, Tang et al. also reported increased CO selectivities on roughened polycrystalline Cu surfaces. Similar to others,⁹ the authors corroborated their experimental results using thermochemical DFT calculations that suggested stronger chemisorption of CO and CHO intermediates on (211) stepped surfaces as compared to planar (100) or (111) surfaces. These predictions are consistent with earlier experimental studies of CO chemisorption on polycrystalline and stepped single crystals of Cu.^{16,73,74} Vollmer et al.¹⁶ reported shifts of CO TPD peaks to higher temperatures as they moved from (111) to (211) and polycrystalline Cu surfaces, indicating stronger CO binding on stepped surface sites. While stepped planar-type surfaces do provide qualitative insight in the effect of steps on reactivity and selectivity, they typically fall short of capturing the more detailed behavior of highly curved NP surfaces.

Another recent computational thermochemical DFT analysis of the CO₂ electroreduction on the stepped Cu(211) surface¹⁴ explored the effect of CO chemisorption on the limiting potential U_L . The limiting potential of an elementary electrochemical reaction step represents the electrochemical overpotential at which the elementary step becomes exergonic (or downhill in free energy), and can be regarded as a simple measure of the potential where the rate of this step becomes appreciable. The elementary step with the largest U_L dictates the overpotential of the overall reaction. Stronger CO binding was predicted to cause a moderate increase in the U_L of the potential-limiting protonation of CO_{ad} according to



This should translate into lower CO protonation rates and lower hydrocarbon selectivities at any constant electrode potential. While this prediction is qualitatively consistent with the present selectivity trends, the dependence of U_L on the CO binding energy appears too weak¹⁴ to account for the sudden selectivity changes in Figure 4.

4.2. Nanoparticle Models. There is a consensus that NP size effects largely originate from size-dependent surface metal atomic coordination and its corresponding surface electronic structure.^{24,26,28,30,33,62,75,76} This is the reason three-dimensional particle models and their surface coordination structure are better suited to help understand particle size effects. A meaningful analysis of surface atomic coordination using particle models requires the selection of structural models that are relevant to the experimental system with respect to size and shape. In the present study, the micelle-assisted, plasma-cleaned NP synthesis initially yielded surface-oxidized Cu NPs, which were subsequently in situ electrochemically reduced to metallic Cu NPs, as confirmed by XPS. Since neither thermal treatments nor repeated potential cycling was applied, the present Cu NPs are rather spherical in shape with only limited surface faceting. Unlike faceted models, spherical particle models also include energetically less favorable, higher-index facets and their characteristic coordination. Clearly, this consideration renders highly faceted Wulff-type particle models inappropriate for the present study, and this is the reason why spherical models with limited faceting were explored in terms of

their surface atomic coordination. Coordination numbers (CN) of surface atoms ranged from 5 to 11, where CN 8 atoms could be largely associated with (100) facets, while CN 9 atoms represented (111) facets, see Figure 5a. The present models also exhibit (110) facets and atoms with CNs of up to 11 (green in Figure 5a).

To understand the observed size effects in Figure 4 in more detail, the experimental trends in catalytic activity and selectivity were correlated with the size-dependent surface structure and coordination in Figure 5.

We start our discussion with the smallest size regime. The smallest Cu NPs S1 and S2 with sizes around 2 nm showed a dramatic increase in overall catalytic activity, which is attributed to the high ratio of low-coordinated surface atoms (CN < 8) starting as low as CN = 5 for NP diameters below 4 nm, see Figure 5b. In this size regime, particle size effects are often referred to as “catalytic finite size effects”, and small variations in size induce drastic changes in the NP’s electronic structure, while quantum effects may become non-negligible.^{28,29,76} Following our arguments on stepped surfaces above, step and kink atoms of Cu NPs with such low CNs are expected to exhibit stronger chemisorption of CO₂, CO, atomic H, and CO_yH_x as compared to larger particles or bulk Cu surfaces. Since the reductive adsorption of protons (the Volmer reaction) on free Cu surface sites ($\text{H}^+ + \text{e}^- + * \rightarrow \text{H}_{\text{ad}}$) is the rate-determining step of the overall electrocatalytic hydrogen evolution reaction (HER),^{77,78} the observed increase in hydrogen production, in hydrogen selectivity, and overall faradaic activity for small NPs appears plausible. A similar argument can be made for those Cu surface orientations where the initial reductive CO₂ adsorption to COOH ($\text{CO}_2 + \text{H}^+ + \text{e}^- + * \rightarrow \text{COOH}_{\text{ad}}$) is rate-determining.^{9,14} Stronger CO₂ adsorption would increase the overall rate of this initial reaction step toward CO.

For Cu particles in the intermediate size range (5–18 nm), the populations of surface atoms with CN = 8 and 9 amount to about 12 and 20%, respectively (see Figure 5b), and remain surprisingly constant over the entire intermediate size range. These population numbers are significantly smaller compared to those found on low-index smooth extended surfaces, such as the (100), (111), or (211) surfaces. With methane and ethylene forming preferentially on (111) (CN = 9) and (100) (CN = 8) sites, respectively,^{3,12,13} changes in the relative populations of (111) and (100) facets provide a plausible explanation for both the sudden steep drop in faradaic selectivities between Cu bulk surfaces and Cu NPs, as well as the selectivity plateau between 2 and 15 nm discernible in Figure 5.

The distinct selectivity observed when comparing small (2 nm) and large (15 nm) NPs can be explained based on the increase in the strength of the binding of products and intermediate reaction species on the smaller NPs. Strong CO binding on low coordinated sites (small NPs) favors high activity, high CO and H₂ selectivities, and reduced hydrocarbon formation. The latter is understood if the reduced surface mobility of the more strongly bound CO_{ad} and H_{ad} on the NP surface is considered, leading to a lower probability of surface reaction to form hydrocarbons. Instead, it is likely that on small NPs CO_{ad} and H_{ad} desorb before reacting on the Cu surface, which explains the higher yields of CO and H₂ products on these samples. The lower mobility of adsorbed intermediate species on the surface of our small spherical NPs can be assigned to their higher curvature and stepped and roughened surfaces. Thus, on the small NPs, the small hydrocarbon yields

detected may be explained based on a different reaction mechanism, as for example, an Eley–Rideal-type one involving the earlier desorption of hydrogen as compared to CO, its diffusion in the liquid phase, readsorption on the Cu surface near a strongly bound CO atom, and subsequent reaction and desorption in the form of a hydrocarbon. For the large NPs, due to the expected weaker CO and H bonding, their diffusivity on the particle surface might be greater, favoring reaction and hydrocarbon formation without having to involve an additional desorption/liquid phase diffusion/readsorption/reaction pathway.

It should also be mentioned here that we do not have any indication of a CO-poisoning effect for the small NP samples. If that were the case, we would have a decrease in the surface area available for water dissociation, which should lead to a decrease in the yield of H₂, which opposes the present observation.

Li and Kanan⁸ recently reported interesting CO₂ electroreduction experiments on Cu oxide electrodes. They achieved significantly increased CO selectivities on electrochemically reduced micrometer-thick Cu oxide films and foils. Following the authors, Cu oxide electroreduction creates a uniquely selective Cu surface. However, for thin Cu oxide layers, this effect vanishes. This is the reason we believe we can exclude the formation of uniquely CO-selective Cu metal phases from Cu oxide particles as origin for the current observations.

In a recent report by Gupta et al.,⁷⁹ the authors highlighted the role of local pH changes during the CO₂ reduction reaction. Under the present experimental conditions, the authors predicted a local pH increase near the electrode surface of about 2 pH units at a Nernst layer thickness of 100 μm. This effect would result in a downshift of the zero point of the RHE scale relative to the NHE scale (and along with it a downshift in the thermodynamic equilibrium potentials of coupled proton/electron half-cell reactions). Given our constant applied electrode potential, this would lead to a decrease in the electrochemical overpotential of proton-coupled electron transfer reactions, leading to a smaller hydrogen evolution rate. This is in obvious conflict with our experimental observations, in which increased hydrogen selectivities and increased current densities were measured for the smallest nanoparticles. We therefore conclude that a strong local pH change is not the origin of the increased faradaic selectivities of hydrogen obtained for our small nanoparticles.

Finally, in recent years, Ono et al.⁸⁰ and subsequently Eckle et al.^{81–83} advanced a particle density based mechanism to account for stability and selectivity changes in NP ensembles. The role of the interparticle distance on the activity and stability of Au NP catalysts during CO oxidation was investigated by Ono et al., and NP samples with larger distances were found to result in lack of reactive-coarsening for these catalysts, while more closely spaced catalysts experienced drastic morphological changes under reaction conditions. Taking the methanation of CO as a model reaction, Eckle et al. argued that low catalyst particle densities favor desorption of intermediates rather than their subsequent reaction by repeated collision with the catalytic surface. We cannot rule out that this effect might also contribute to the present observations. While in our study the particle density of the most H₂- and CO-selective particle ensembles (smaller size Cu NPs, S1 and S2) is larger than that of the larger Cu NPs (S6) which were found to be less CO-selective, the samples with the smallest NPs also have the smallest total Cu surface coverage (see Table 1). Therefore, readsorption and reaction should also be less

favorable on our smallest NP samples. This is an interesting aspect that requires further attention and will be addressed in a separate study where we are systematically changing the interparticle distance while keeping the particle size constant.

In summary, a spherical particle model provided valuable insight into experimental trends in activity and selectivity of CO₂ electroreduction as a function of particle size. An increasing number of surface atoms with CN below 8 are responsible for enhanced hydrogen and CO evolution on NPs around 2 nm and below. Characteristic changes in the populations of low coordinated sites provide plausible explanations for experimental activity and selectivity variations for NPs between 5 and 15 nm. The smallest Cu NPs at and below 2 nm displayed the most drastic dependence of product selectivities on particle size consistent with a dramatic increase in the content of low-coordinated surface atoms.

5. CONCLUSION

The particle size effect has been explored for the catalytic electroreduction of CO₂ on Cu NPs in the size range of 2–15 nm and compared to bulk Cu. Given that this reaction is emerging as one of the most important processes for chemical storage of electricity, knowledge about the reactivity and selectivity of this reaction on nanoscale catalysts is of utmost importance.

Nanometer-sized Cu NPs showed a dramatic increase in overall catalytic activity (faradaic current). Selectivity analysis has revealed that enhanced formation of CO and H₂ accounts for the increase in the faradaic activity observed on the Cu NPs. The selectivity of hydrocarbons first changed to a reduced constant plateau, until it virtually vanished for NP sizes at and below 2 nm.

A model of *nonfaceted, spherical*, and hence experimentally relevant, Cu particles was used to estimate the population of surface atoms with specific coordination numbers. Below 2 nm, a drastic increase in under-coordinated atoms with CN < 8 is observed. These strongly binding sites accelerate the hydrogen evolution and the CO₂ reduction to CO. However, they seem to be unfavorable for the subsequent hydrogenation of CO, which lowers hydrocarbon selectivity at small particles. A plausible explanation for the observed trend is the reduced mobility of intermediate reaction species (CO and H) on the small NPs due to their stronger bonding, which decreases the chance of further recombination and reaction to form hydrocarbons on the Cu surface.

At intermediate particle sizes, the spherical particle model predicts low and constant populations of (100) and (111) facets, which is consistent with the reduced, yet constant hydrocarbon selectivities observed for Cu NPs between 5 and 15 nm compared to Cu bulk surfaces. For these larger NPs, weaker binding of CO and H is expected, favoring hydrocarbon formation.

Overall, the presented size-dependent selectivity conclusions help obtain a more complete mechanistic understanding of the CO₂ electroreduction process. Catalyst materials, their geometry, and the reaction conditions lend themselves easily to DFT theoretical verification and refined mechanistic interpretation. In particular, this study considers particles below 2 nm, which have become computationally tractable by theorists using *ab initio* codes. This opens the possibility for further in-depth DFT work on the present system.

Clearly, where hydrocarbon yields are of the essence, very small (<3 nm) nanoscale Cu catalysts should be avoided.

However, where syngas is the preferred reaction product, for instance, to serve as feed for gas-to-liquid reaction technologies, the size of the Cu particles could serve as a convenient parameter to deliberately control the resulting H₂ to CO product ratio.

■ ASSOCIATED CONTENT

📄 Supporting Information

XPS data from the C-1s region, TEM data and the corresponding histogram obtained from sample S1; histograms of nanoparticle heights obtained from AFM; an overview of catalytic activity and product distribution, schematic illustration of the used GC method, number of atoms and surface population as a function of NP diameter for spherical FCC Cu model shapes, and the Tafel characteristics for all samples. This material is available free of charge via the Internet at <http://pubs.acs.org>.

■ AUTHOR INFORMATION

Corresponding Authors

pstrasser@tu-berlin.de
Beatriz.Roldan@rub.de

Author Contributions

^{||}These authors contributed equally.

Notes

The authors declare no competing financial interest.

■ ACKNOWLEDGMENTS

The authors thank Dr. Lin Gan from TU Berlin for the acquisition of TEM data. We thank Dr. Ana Varela for helpful discussions. H.M., F.B., and B.R.C. (UCF and RUB) acknowledge funding from the U.S. Department of Energy DOE-BES (DE-FG02-08ER15995). B.R.C. acknowledges financial support by the cluster of excellence RESOLV (DFG, EXC-1069) at the Ruhr University Bochum. We thank the “Zentraleinrichtung für Elektronenmikroskopie (Zelmi)” of the Technical University Berlin for their support with TEM techniques. Financial support by the German Research Foundation (DFG) through Grant STR 596/3-1 under the Priority Program 1613 “Regeneratively formed fuels by water splitting” is gratefully acknowledged.

■ REFERENCES

- (1) Schwartz, S. E. *Energy Environ. Sci.* **2008**, *1*, 430.
- (2) Aresta, M. *Carbon Dioxide as Chemical Feedstock*; Wiley: Weinheim, 2010.
- (3) Hori, Y. In *Modern Aspects of Electrochemistry*; Vayenas, C. G., Ed.; Springer: New York, 2008; p 89.
- (4) Hori, Y.; Murata, A.; Takahashi, R. *J. Chem. Soc., Faraday Trans. 1* **1989**, *85*, 2309.
- (5) Gattrell, M.; Gupta, N.; Co, A. *J. Electroanal. Chem.* **2006**, *594*, 1.
- (6) Hori, Y.; Takahashi, R.; Yoshinami, Y.; Murata, A. *J. Phys. Chem. B* **1997**, *101*, 7075.
- (7) Durand, W. J.; Peterson, A. A.; Studt, F.; Abild-Pedersen, F.; Norskov, J. K. *Surf. Sci.* **2011**, *605*, 1354.
- (8) Li, C. W.; Kanan, M. W. *J. Am. Chem. Soc.* **2012**, *134*, 7231.
- (9) Peterson, A. A.; Abild-Pedersen, F.; Studt, F.; Rossmeisl, J.; Norskov, J. K. *Energy Environ. Sci.* **2010**, *3*, 1311.
- (10) Tang, W.; Peterson, A. A.; Varela, A. S.; Jovanov, Z. P.; Bech, L.; Durand, W. J.; Dahl, S.; Norskov, J. K.; Chorkendorff, I. *Phys. Chem. Chem. Phys.* **2012**, *14*, 76.
- (11) Nie, X.; Esopi, M. R.; Janik, M. J.; Asthagiri, A. *Angew. Chem., Int. Ed.* **2013**, *52*, 2459.

- (12) Schouten, K. J. P.; Kwon, Y.; van der Ham, C. J. M.; Qin, Z.; Koper, M. T. M. *Chem. Sci.* **2011**, *2*, 1902.
- (13) Schouten, K. J. P.; Qin, Z.; Gallent, E. P.; Koper, M. T. M. *J. Am. Chem. Soc.* **2012**, *134*, 9864.
- (14) Peterson, A. A.; Norskov, J. K. J. *Phys. Chem. Lett.* **2012**, *3*, 251.
- (15) Christophe, J.; Doneux, T.; Buess-Herman, C. *Electrocatalysis* **2012**, *3*, 139.
- (16) Vollmer, S.; Witte, G.; Wöll, C. *Catal. Lett.* **2001**, *77*, 97.
- (17) Mavrikakis, M.; Hammer, B.; Norskov, J. K. *Phys. Rev. Lett.* **1998**, *81*, 2819.
- (18) Molodkina, E. B.; Ehrenburg, M. R.; Polukarov, Y. M.; Danilov, A. I.; Souza-Garcia, J.; Feliu, J. M. *Electrochim. Acta* **2010**, *56*, 154.
- (19) Oezaslan, M.; Hasche, F.; Strasser, P. *J. Electrochem. Soc.* **2012**, *159*, B444.
- (20) Strasser, P.; Koh, S.; Anniyev, T.; Greeley, J.; More, K.; Yu, C.; Liu, Z.; Kaya, S.; Nordlund, D.; Ogasawara, H.; Toney, M. F.; Nilsson, A. *Nat. Chem.* **2010**, *2*, 454.
- (21) Reske, R.; Duca, M.; Oezaslan, M.; Schouten, K. J. P.; Koper, M. T. M.; Strasser, P. *J. Phys. Chem. Lett.* **2013**, *4*, 2410.
- (22) Gasteiger, H. A.; Kocha, S. S.; Sompalli, B.; Wagner, F. T. *Appl. Catal., B* **2005**, *56*, 9.
- (23) Mukerjee, S. *J. Appl. Electrochem.* **1990**, *20*, 537.
- (24) Arai, M. *J. Chem. Eng. Jpn.* **1997**, *30*, 1123.
- (25) Coq, B.; Figueras, F. *Coord. Chem. Rev.* **1998**, *178*, 1753.
- (26) Bond, G. C. *Surf. Sci.* **1985**, *156*, 966.
- (27) Ono, L. K.; Croy, J. R.; Heinrich, H.; Roldan Cuenya, B. *J. Phys. Chem. C* **2011**, *115*, 16856.
- (28) Li, L.; Larsen, A. H.; Romero, N. A.; Morozov, V. A.; Glinsvad, C.; Abild-Pedersen, F.; Greeley, J.; Jacobsen, K. W.; Norskov, J. K. *J. Phys. Chem. Lett.* **2013**, *4*, 222.
- (29) Kleis, J.; Greeley, J.; Romero, N. A.; Morozov, V. A.; Falsig, H.; Larsen, A. H.; Lu, J.; Mortensen, J. J.; Dulak, M.; Thygesen, K. S.; Norskov, J. K.; Jacobsen, K. W. *Catal. Lett.* **2011**, *141*, 1067.
- (30) Tritsarlis, G.; Greeley, J.; Rossmel, J.; Norskov, J. *Catal. Lett.* **2011**, *141*, 909.
- (31) Bezemer, G. L.; Bitter, J. H.; Kuipers, H. P. C. E.; Oosterbeek, H.; Holeywijn, J. E.; Xu, X. D.; Kapteijn, F.; van Dillen, A. J.; de Jong, K. P. *J. Am. Chem. Soc.* **2006**, *128*, 3956.
- (32) den Breejen, J. P.; Radstake, P. B.; Bezemer, G. L.; Bitter, J. H.; Froseth, V.; Holmen, A.; de Jong, K. P. *J. Am. Chem. Soc.* **2009**, *131*, 7197.
- (33) Argo, A. M.; Odzak, J. F.; Gates, B. C. *J. Am. Chem. Soc.* **2003**, *125*, 7107.
- (34) Jacobsen, C. J. H.; Dahl, S.; Hansen, P. L.; Tornqvist, E.; Jensen, L.; Topsoe, H.; Prip, D. V.; Moenshaug, P. B.; Chorkendorff, I. *J. Mol. Catal. A: Chem.* **2000**, *163*, 19.
- (35) Croy, J. R.; Mostafa, S.; Liu, J.; Sohn, Y.-h.; Cuenya, B. *Catal. Lett.* **2007**, *118*, 1.
- (36) Subramanian, V.; Wolf, E. E.; Kamat, P. V. *J. Am. Chem. Soc.* **2004**, *126*, 4943.
- (37) Gucci, L.; Beck, A.; Paszti, Z. *Catal. Today* **2012**, *181*, 26.
- (38) Ishida, T.; Kinoshita, N.; Okatsu, H.; Akita, T.; Takei, T.; Haruta, M. *Angew. Chem., Int. Ed.* **2008**, *47*, 9265.
- (39) Haruta, M. *Relevance of Metal Nanoclusters Size Control in Gold(0) Catalytic Chemistry*; Elsevier Science Bv: Amsterdam, 2008.
- (40) Haruta, M. *Size- and Support-Dependency in the Catalysis of Noble Metals: Gold as a Typical Example*; Imperial College Press: London, 2001; Vol. 117.
- (41) Cunningham, D. A. H.; Vogel, W.; Kageyama, H.; Tsubota, S.; Haruta, M. *J. Catal.* **1998**, *177*, 1.
- (42) Kumar, S.; Zou, S. Z. *Langmuir* **2009**, *25*, 574.
- (43) Overbury, S. H.; Schwartz, V.; Mullim, D. R.; Yan, W. F.; Dai, S. *J. Catal.* **2006**, *241*, 56.
- (44) Haruta, M.; Tsubota, S.; Kobayashi, T.; Kageyama, H.; Genet, M. J.; Delmon, B. *J. Catal.* **1993**, *144*, 175.
- (45) Heiz, U.; Sanchez, A.; Abbet, S.; Schneider, W. D. *J. Am. Chem. Soc.* **1999**, *121*, 3214.
- (46) Chin, Y. H.; Iglesia, E. *J. Phys. Chem. C* **2011**, *115*, 17845.
- (47) Bond, G. C. *Molecules* **2012**, *17*, 1716.
- (48) Ono, L. K.; Sudfeld, D.; Roldan Cuenya, B. *Surf. Sci.* **2006**, *600*, 5041.
- (49) Kinoshita, K. *J. Electrochem. Soc.* **1990**, *137*, 845.
- (50) Mayrhofer, K. J. J.; Blizanac, B. B.; Arenz, M.; Stamenkovic, V. R.; Ross, P. N.; Markovic, N. M. *J. Phys. Chem. B* **2005**, *109*, 14433.
- (51) Shao, M. H.; Peles, A.; Shoemaker, K. *Nano Lett.* **2011**, *11*, 3714.
- (52) Nesselberger, M.; Ashton, S.; Meier, J. C.; Katsounaros, I.; Mayrhofer, K. J. J.; Arenz, M. *J. Am. Chem. Soc.* **2011**, *133*, 17428.
- (53) Mukejee, S.; McBreen, J. *J. Electroanal. Chem.* **1998**, *448*, 163.
- (54) Corradini, P. G.; Pires, F. I.; Paganin, V. A.; Perez, J.; Antolini, E. *J. Nanopart. Res.* **2012**, *14*, No. 1080.
- (55) Jirkovský, J.; Makarova, M.; Krtíl, P. *Electrochem. Commun.* **2006**, *8*, 1417.
- (56) Jirkovský, J.; Hoffmannová, H.; Klementová, M.; Krtíl, P. *J. Electrochem. Soc.* **2006**, *153*, E111.
- (57) Kwon, G.; Ferguson, G. A.; Heard, C. J.; Tyo, E. C.; Yin, C. R.; DeBartolo, J.; Seifert, S.; Winans, R. E.; Kropf, A. J.; Greeley, J.; Johnston, R. L.; Curtiss, L. A.; Pellin, M. J.; Vajda, S. *ACS Nano* **2013**, *7*, 5808.
- (58) Reier, T.; Oezaslan, M.; Strasser, P. *ACS Catal.* **2012**, *2*, 1765.
- (59) Park, S.; Xie, Y.; Weaver, M. J. *Langmuir* **2002**, *18*, 5792.
- (60) Diao, P.; Zhang, D. F.; Guo, M.; Zhang, Q. *J. Catal.* **2007**, *250*, 247.
- (61) Jaramillo, T. F.; Baek, S.-H.; Cuenya, B. R.; McFarland, E. W. *J. Am. Chem. Soc.* **2003**, *125*, 7148.
- (62) Roldan Cuenya, B.; Baek, S.-H.; Jaramillo, T. F.; McFarland, E. W. *J. Am. Chem. Soc.* **2003**, *125*, 12928.
- (63) Watanabe, M.; Sei, H.; Stonehart, P. *J. Electroanal. Chem.* **1989**, *261*, 375.
- (64) Merte, L. R.; Behafarid, F.; Miller, D. J.; Friebel, D.; Cho, S.; Mbuga, F.; Sokaras, D.; Alonso-Mori, R.; Weng, T.-C.; Nordlund, D. *ACS Catal.* **2012**, *2*, 2371.
- (65) Firsova, A. A.; Khomenko, T. I.; Il'ichev, A. N.; Korchak, V. N. *Kinet. Catal.* **2011**, *52*, 434.
- (66) Liou, Y. H.; Lo, S. L.; Lin, C. J. *Water Res.* **2007**, *41*, 1705.
- (67) Ono, L.; Yuan, B.; Heinrich, H.; Cuenya, B. *J. Phys. Chem. C* **2010**, *114*, 22119.
- (68) Croy, J. R.; Mostafa, S.; Heinrich, H.; Roldan Cuenya, B. *Catal. Lett.* **2009**, *131*, 21.
- (69) Mostafa, S.; Behafarid, F.; Croy, J. R.; Ono, L. K.; Li, L.; Yang, J. C.; Frenkel, A. I.; Roldan Cuenya, B. *J. Am. Chem. Soc.* **2010**, *132*, 15714.
- (70) Roldan Cuenya, B. *Thin Solid Films* **2010**, *518*, 3127.
- (71) Kuhl, K. P.; Cave, E. R.; Abram, D. N.; Jaramillo, T. F. *Energy Environ. Sci.* **2012**, *5*, 7050.
- (72) Hori, Y.; Takahashi, I.; Koga, O.; Hoshi, N. *J. Mol. Catal.* **2003**, *199*, 39.
- (73) Xu, X. P.; Vesecky, S. M.; He, J. W.; Goodman, D. W. *J. Vac. Sci. Technol., A* **1993**, *11*, 1930.
- (74) Xu, X. P.; He, J. W.; Goodman, D. W. *Surf. Sci.* **1993**, *284*, 103.
- (75) Behafarid, F.; Ono, L.; Mostafa, S.; Croy, J.; Shafai, G.; Hong, S.; Rahman, T.; Bare, S. R.; Cuenya, B. *J. Phys. Chem. Chem. Phys.* **2012**, *14*, 11766.
- (76) Greeley, J.; Rossmel, J.; Hellman, A.; Norskov, J. K. *Z. Phys. Chem.* **2007**, *221*, 1209.
- (77) Norskov, J. K.; Bligaard, T.; Logadottir, A.; Kitchin, J. R.; Chen, J. G.; Pandelov, S.; Stimming, U. *J. Electrochem. Soc.* **2005**, *152*, J23.
- (78) Greeley, J.; Kibler, L.; El-Aziz, A. M.; Kolb, D. M.; Norskov, J. K. *ChemPhysChem* **2006**, *7*, 1032.
- (79) Gupta, N.; Gattrell, M.; MacDougall, B. *J. Appl. Electrochem.* **2006**, *36*, 161.
- (80) Ono, L. K.; Roldan Cuenya, B. *Catal. Lett.* **2007**, *113*, 86.
- (81) Eckle, S.; Denkwitz, Y.; Behm, R. J. *J. Catal.* **2010**, *269*, 255.
- (82) Eckle, S.; Augustin, M.; Anfang, H. G.; Behm, R. J. *Catal. Today* **2012**, *181*, 40.
- (83) Eckle, S.; Anfang, H. G.; Behm, R. J. *Appl. Catal., A* **2011**, *391*, 325.